



A hydrous melting and fractionation model for mid-ocean ridge basalts: Application to the Mid-Atlantic Ridge near the Azores

P. D. Asimow

*Division of Geological and Planetary Sciences, California Institute of Technology, Pasadena, California 91125, USA
(asimow@gps.caltech.edu)*

Formerly at Lamont-Doherty Earth Observatory, Palisades, New York 10964, USA

J. E. Dixon

*Rosenstiel School of Marine and Atmospheric Science, Division of Marine Geology and Geophysics, University of Miami, Miami, Florida 33149, USA
(jdixon@rsmas.miami.edu)*

C. H. Langmuir

Lamont-Doherty Earth Observatory, Palisades, New York 10964, USA

*Now at Department of Earth and Planetary Sciences, Harvard University, Cambridge, Massachusetts 02138, USA
(langmuir@eps.harvard.edu)*

[1] The major element, trace element, and isotopic composition of mid-ocean ridge basalt glasses affected by the Azores hotspot are strongly correlated with H₂O content of the glass. Distinguishing the relative importance of source chemistry and potential temperature in ridge-hotspot interaction therefore requires a comprehensive model that accounts for the effect of H₂O in the source on melting behavior and for the effect of H₂O in primitive liquids on the fractionation path. We develop such a model by coupling the latest version of the MELTS algorithm to a model for partitioning of water among silicate melts and nominally anhydrous minerals. We find that much of the variation in all major oxides except TiO₂ and a significant fraction of the crustal thickness anomaly at the Azores platform are explained by the combined effects on melting and fractionation of up to ~700 ppm H₂O in the source with only a small thermal anomaly, particularly if there is a small component of buoyantly driven active flow associated with the more H₂O-rich melting regimes. An on-axis thermal anomaly of ~35°C in potential temperature explains the full crustal thickness increase of ~4 km approaching the Azores platform, whereas a ≥75°C thermal anomaly would be required in the absence of water or active flow. The polybaric hydrous melting and fractionation model allows us to solve for the TiO₂, trace element and isotopic composition of the H₂O-rich component in a way that self-consistently accounts for the changes in the melting and fractionation regimes resulting from enrichment, although the presence and concentration in the enriched component of elements more compatible than Dy cannot be resolved.

Components: 13,623 words, 8 figures, 1 table.

Keywords: Mid-Atlantic Ridge; Azores; basalt fractionation; hydrous mantle melting; plume-ridge interaction.

Index Terms: 3640 Mineralogy and Petrology: Igneous petrology; 3035 Marine Geology and Geophysics: Midocean ridge processes; 9325 Information Related to Geographic Region: Atlantic Ocean.

Received 11 April 2003; **Revised** 21 October 2003; **Accepted** 18 November 2003; **Published** 28 January 2004.



Asimow, P. D., J. E. Dixon, and C. H. Langmuir (2004), A hydrous melting and fractionation model for mid-ocean ridge basalts: Application to the Mid-Atlantic Ridge near the Azores, *Geochem. Geophys. Geosyst.*, 5, Q01E16, doi:10.1029/2003GC000568.

Theme: Plume-Ridge Interaction **Guest Editor:** David Graham

1. Introduction

[2] Variations in the trace element ratios and isotopic composition of basalts collected along the Mid-Atlantic Ridge generally reveal long-wavelength patterns associated with proximity to hotspots [Schilling *et al.*, 1983], including Jan Mayen [Schilling *et al.*, 1999], Iceland [Hart *et al.*, 1973], the Azores [Schilling, 1975], Sierra Leone [Schilling *et al.*, 1994], Shona and Discovery [Douglass *et al.*, 1995, 1999], the Tristan da Cunha group [Humphris *et al.*, 1985; Hanan *et al.*, 1986], and Bouvet [Dickey *et al.*, 1977; LeRoex *et al.*, 1987]. Distinguishing the thermal and chemical effects of hotspots on mid-ocean ridges, determining the composition of the hotspot-related components, and understanding the geodynamic processes that disperse hotspot material over ~1000 km distances have become both the principal barriers to global understanding of ridge dynamics and essential areas of opportunity for deep understanding of the earth's interior.

[3] It has long been a matter of debate whether the Azores, in particular, are principally the result of a thermal hotspot or a compositional anomaly, perhaps a "wet spot" [Bonatti, 1990]. The shallow bathymetry of the ridge axis across the Azores platform certainly requires a low-density column relative to normal zero-age oceanic lithosphere, and this is most easily achieved by thickening of the crust, as is indeed observed seismically [Searle, 1976]. A thick oceanic crust, in turn, requires either higher-than-normal extents of melting or the processing of extra mantle through the melting regime by an active flow field. Both high extents of melting and anomalous buoyancy and/or viscosity (needed to drive active flow), however, are consistent either with elevated mantle temperatures or volatile-enriched source compositions. Schilling

[1975] documented large enrichments of light rare earth elements along the ridge approaching the Azores and concluded a chemically enriched source was required because melting and fractionation processes were inadequate to explain the patterns (indeed, this would require much smaller degrees of melting in the enriched samples, which makes the crustal volume anomaly that much harder to explain, Hofmann and White [1982]). Suggestions for the origin of this enriched domain have included subducted, partially dehydrated oceanic crust [Hofmann and White, 1982; Kurz *et al.*, 1982] or fragments of continental lithosphere either left behind during the opening of the Atlantic [Bonatti, 1971] or delaminated and later advected upward in a plume [McKenzie and O'Nions, 1983, 1995]. Noble gas evidence from the Azores and the nearby mid-Atlantic Ridge have been interpreted in terms of three component mixing, requiring both an undegassed and a recycled component [Moreira and Allègre, 1999]. Bonatti [1990] examined the mineral chemistry and equilibration temperatures of abyssal peridotites from the Azores region and found higher extents of depletion (complementary to high extents of melting) than elsewhere in the Atlantic, but equal or cooler temperatures.

[4] Given the complex interplay of source composition, potential temperature, melting process, mixing of melt increments, and fractionation effects in determining the composition and volume of mid-ocean ridge crust, progress in separating these effects requires the application of a model through which hypotheses can be realized and compared to data. The model must be sufficiently powerful to account for all the sources of variability that are potentially of interest, and it ought to be sufficiently accurate to provide confidence in the results. Given that many aspects of the melting process are unobservable, such models are difficult to test



completely. Hence it is best to use a model that accounts for a wide range of experimental constraints and that is based on thermodynamic principles. Comprehensive models of mid-ocean ridge basalt production based on empirical [McKenzie and Bickle, 1988; Niu and Batiza, 1991; Langmuir *et al.*, 1992; Kinzler, 1997] or thermodynamic parameterization [Asimow *et al.*, 2001] have led to much insight into the depths of origin of mid-ocean ridge magmas, the range of mantle potential temperature, the variability in mantle source compositions, the effects of the melt transport process on re-equilibration and mixing, and other issues.

[5] All of the comprehensive models applied to date, however, share the limitation that they consider only anhydrous conditions. Yet for a number of reasons there has been renewed interest in considering the role of H₂O in determining the melting behavior of the MORB source region. The interpretation of seismic evidence suggesting a small fraction of melt beneath the southern East Pacific Rise [MELT Seismic Team, 1998] at pressures higher than those consistent with anhydrous models suggests water is important even in normal ridge segments. Certainly to understand a water-enriched study area such as the Azores region, we need a model that includes H₂O. Although the direct effects of H₂O on melting [Yoder and Tilley, 1962; Kushiro, 1972; Green, 1973; Kushiro, 1975; Green, 1976; Stolper and Newman, 1994; Hirose and Kawamoto, 1995; Gaetani and Grove, 1998; Falloon and Danyushevsky, 2000] and fractionation [Michael and Chase, 1987; Sinton and Fryer, 1987; Danyushevsky, 2001] are fairly well-understood, no comprehensive model of mid-ocean ridge petrogenesis that accounts for H₂O in the source and in the primary liquid exists. We have developed such a model by extending a previous anhydrous model [Asimow *et al.*, 2001] based on the MELTS algorithm of Ghiorso and Sack [1995] to include a description of the partitioning of water between nominally anhydrous mantle minerals and basaltic melts [Hirth and Kohlstedt, 1996]. For the melting part of the calculation we have adopted a recent recalibration of the silicate liquid model optimized for peridotite melting at high pressure, known as pMELTS [Ghiorso *et al.*, 2002], but the

fractionation step uses the original MELTS calibration, which is more accurate at low pressure. We present the development and implementation of this new hybrid model (pHMELTS) and then show its implications for petrogenesis in the Atlantic based on the FAZAR cruise data (Atlantis II cruise 127; full sample documentation to be presented in a separate paper in this journal; Asimow *et al.*, in preparation, 2003). This model demonstrates good agreement with an independently developed extension of the Langmuir *et al.* [1992] anhydrous ridge model and both models show the interesting behavior that H₂O addition to the source causes decreasing mean extents of melting with increasing total melt production and hence requires less enriched sources and smaller temperature anomalies at the Azores and the Galápagos spreading center than would be required by anhydrous models [Asimow and Langmuir, 2003].

2. Development of Wet Melting Model

[6] Given the high water contents of basalts from the study area and the well-known effects of H₂O on both melting and fractionation, a necessary first step in understanding the relationship between source heterogeneity and observables must be a forward model of MORB production and fractionation in the presence of H₂O. All published models of MORB melting that account for polybaric melt production and mixing to produce a primary aggregate melt [Klein and Langmuir, 1987; McKenzie and Bickle, 1988; Niu and Batiza, 1991; Kinzler and Grove, 1992; Langmuir *et al.*, 1992; Kinzler, 1997; Asimow *et al.*, 2001] to date have been anhydrous models. Most work on hydrous melting has focused on the water-rich subduction zone environment. For the water-poor, yet not completely anhydrous, ridge environment, a new model is needed. We chose to base pHMELTS on the pMELTS calibration in part because it incorporates the Pitzer and Sterner [1994] equation of state for H₂O, which extrapolates well to high pressure, as opposed to the Haar *et al.* [1984] equation used in MELTS, which fails at 1.0 GPa.

[7] The consensus among mineralogists and mineral physicists [Bai and Kohlstedt, 1992; Bell and



Rossmann, 1992; Karato and Jung, 1998] is that H₂O in the upper mantle at concentrations up to about one thousand parts per million (ppm) by weight is stored in the nominally anhydrous minerals olivine, pyroxenes, and garnet. pMELTS has the ability to model the effect of H₂O dissolved in the liquid phase. In the absence of hydrous phases such as free vapor or amphiboles, however, it knows no location other than the liquid to store H₂O and so cannot be used to find the water-undersaturated solidus or to perform water-undersaturated fractional melting calculations. We worked around this limitation by adopting the model of Hirth and Kohlstedt [1996] for solubility of H₂O in olivine and relative partitioning of H₂O among mantle solids. In this model the solubility of H₂O in olivine is proportional to the standard-state fugacity of water $f_{H_2O}^o$. We retain their assumption of Henry's law behavior for H₂O in the solids such that, at constant $f_{H_2O}^o$, concentration is proportional to activity of H₂O, a_{H_2O} . Hirth and Kohlstedt [1996] further assumed that the solubility of H₂O in the melt is proportional to $(f_{H_2O}^o)^{1/2}$ but that at constant pressure and temperature water concentration in the melt is linearly proportional to a_{H_2O} . These assumptions taken together yield a partition coefficient D_{H_2O} that is equal to the ratio of solubilities, is independent of water content, and depends only on pressure and temperature. Our model differs from Hirth and Kohlstedt's [1996] treatment in two ways. First, we use the solubility of water in the liquid phase implicit in pMELTS rather than a simple dependence on $(f_{H_2O}^o)^{1/2}$; this accounts for any dependence of water solubility on melt composition that may arise in the pMELTS calibration. Second, since at low concentrations H₂O dissolves in melt as two OH groups, we do not assume Henry's law for H₂O concentration in the melt, which makes our D_{H_2O} depend on concentration as well as pressure and temperature. In particular, just as the solubility of H₂O in the melt depends on $(f_{H_2O}^o)^{1/2}$, so the concentration of H₂O in the melt when water is undersaturated should depend on $(f_{H_2O}^o)^{1/2} = (a_{H_2O})^{1/2} (f_{H_2O}^o)^{1/2}$. Only at saturation, when $a_{H_2O} = 1$ and fugacity is equal to standard-state fugacity, does this model give the same result as

Hirth and Kohlstedt's assumptions. Thus our model, by adopting a convention that makes the water content in melt when water-undersaturated thermodynamically consistent with the solubility model, introduces an additional dependence of the partition coefficient on $(a_{H_2O})^{1/2}$. As we will see below, this makes H₂O partitioning concentration-dependent, such that H₂O is more compatible in more H₂O-rich source compositions, and such that D_{H_2O} decreases rapidly during near-fractional decompression melting due both to decreasing pressure and decreasing concentration.

[8] To detect the solidus and the onset of melting with this model, we adopted an approach analogous to the method described by Ghiorso [1985] for calculation of equilibrium at fixed f_{O_2} . We construct and minimize a Korzhinskii-type potential that fixes the activity of H₂O rather than the water content of the system. Given the assumed Henrian behavior of H₂O in the solids, the activity of H₂O below the solidus is determined as follows. First H₂O is partitioned among the various minerals to obtain the concentration in olivine. The solubility of H₂O in olivine is taken from Hirth and Kohlstedt's function of the fugacity of pure water at the pressure and temperature of interest. Then the activity is given by the ratio of water concentration in olivine to water solubility in olivine. Since the activity of water depends on the modal abundance of the minerals, an iteration is required to find an equilibrium mineral assemblage and a_{H_2O} that are consistent with the desired bulk water content. Then, given the activities of all the major components from the calculation of equilibrium and the activity of H₂O from the concentration in olivine relative to its solubility, we test for the saturation of the non-ideal pMELTS silicate liquid phase using the algorithm described by Ghiorso [1994] as modified by Asimow and Ghiorso [1998].

[9] Figure 1 shows the solidus relations predicted by pMELTS for our adopted depleted end member composition, including the dry and water-saturated solidus curves, solidus contours of equal water activity, and solidus curves at fixed bulk H₂O contents. See below for the details of this source composition; it is obtained from fertile peridotite by removing ~1% melt. The boundaries of the

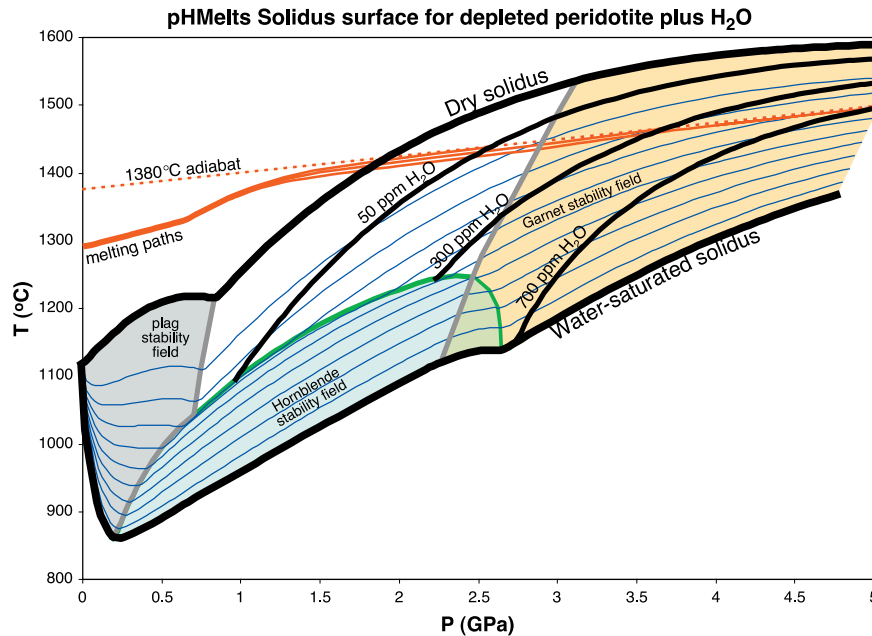


Figure 1. Solidus relations for our adopted depleted peridotite composition (Table 1) with variable H₂O contents as predicted by the pHMELTS model, a hybrid of pMELTS [Ghiorso *et al.*, 2002] and the estimates of solubility of water in nominally anhydrous minerals given by Hirth and Kohlstedt [1996]. The upper heavy black curve is the anhydrous solidus ($a_{H_2O} = 0$); the lowermost heavy black curve is the water-saturated solidus ($a_{H_2O} = 1$). The blue contours in between are lines of constant activity of water on the solidus at increments of 0.1 in a_{H_2O} . The black curves labeled 50, 300, and 700 show the solidus predicted for these bulk H₂O contents in parts per million by weight. These are not parallel to the activity contours because the increase with pressure in the solubility of H₂O in the solid mineral assemblage implies a decrease in a_{H_2O} at fixed bulk water content with increasing pressure. The gray lines delimit the stability of garnet and plagioclase on the solidus respectively; spinel is present everywhere because of the Cr₂O₃ component [see Asimow *et al.*, 1995]. The green boundary delimits the stability of hornblende on the solidus; this is probably not predicted well given the simple thermodynamic model of hornblende currently available and occupies a temperature too low for interest at mid-ocean ridges, but is shown for completeness. The dotted red line is the solid adiabat with potential temperature 1380°C; it is metastable once melting begins. The solid red curves are the pressure-temperature trajectories of the adiabatic continuous melting paths for 50, 300, and 700 ppm bulk H₂O in the source.

plagioclase, garnet, and hornblende stability fields on the solidus are also shown. Note that the solidus contours for 50 and 300 ppm bulk water do not enter the hornblende stability field but instead follow its boundary; were the potential temperature low enough to stabilize amphibole peridotite, then the solidus at these water concentrations would be defined by dehydration melting at the breakdown of hornblende. For potential temperatures appropriate to normal oceanic mantle, the adiabat does not intersect this field and melting begins at a point on an undersaturated solidus contour defined by the water content and potential temperature. Thus for example, the dashed red curve shows the 1380°C adiabat and the solid red curves show three melting paths beginning on this adiabat for

assemblages with 50, 300, and 700 ppm H₂O. As pressure decreases and the water concentration necessary to saturate the nominally anhydrous mineral assemblage decreases, the solidus contours at fixed bulk water content each merge with the water-saturated solidus. Figure 1 is qualitatively similar to the corresponding solidus relations shown by Hirth and Kohlstedt [1996] based on their interpolation between estimated dry and water-saturated solidi.

[10] As the pHMELTS calculation continues beyond the initiation of melting, an additional accounting trick is required that tracks H₂O dissolved in the solids separately from the bulk composition input to pMELTS for equilibration,



since pMELTS only knows about the water that is dissolved in the liquid phase. This is accomplished using a trace element add-on to pMELTS that, given a set of mineral-melt partition coefficients and an initial bulk concentration of each trace element, calculates bulk partition coefficients from the modes obtained by pMELTS and distributes trace elements accordingly. Hence given an initial guess of the melt fraction, the trace element subroutine calculates how much water should be in the melt phase according to the mineral solubility models of Hirth and Kohlstedt and adjusts the bulk composition considered by pMELTS. Since the mass of H₂O in the liquid phase depends on melt fraction and the melt fraction depends on the mass of dissolved H₂O, iteration is required to find thermal, major, and trace element equilibrium. When this iteration converges, the total H₂O content of minerals and melt equals the prescribed bulk H₂O content, the system is in thermodynamic equilibrium and, in particular, the activity of H₂O implied by the water content of the minerals equals the a_{H_2O} implied by the water content of the melt. This iteration has been made computationally efficient enough that a melting column from 4 GPa to the surface in 0.01 GPa steps can be calculated in a few minutes on a workstation.

[11] The pHMELTS model is used to calculate primary liquid compositions following the approach described in detail in *Asimow et al.* [2001]. We simulate continuous melting in this work by decompressing the assemblage isentropically until the melt fraction by volume exceeds 1%. Any fraction of liquid above 1% is then extracted and the entropy of the remaining system is used as the reference for the next decompression step. This continuous melting approach differs from the perfect fractional melting treatments in *Asimow et al.* [2001] and *Asimow and Langmuir* [2003]; we adopted it here mostly to avoid the need for calculations at extreme pressures beyond the reasonable calibrated range of pMELTS. The behavior of water in this model and its effect upon melting are demonstrated in Figure 2. Figure 2a compares the melt productivity, percent increase in degree of melting per kbar pressure decrease, of the dry

pMELTS model and the pHMELTS model at equal potential temperature and various water contents. The major features of these productivity functions include a low near-solidus productivity, increasing to a maximum of about 3%/kbar just before the exhaustion of cpx from the residue, followed by a drop to values <1.5%/kbar for harzburgite melting [*Asimow et al.*, 1997, 2001]. Compared to previously published MELTS productivity curves for fertile peridotite, the dry solidus productivity is higher and the low-productivity tail much shorter for this depleted source composition. The pHMELTS productivity curves show that the productivity of water-induced melting below the dry solidus, about 0.1%/kbar, is lower than the initial productivity of dry melting. Figure 2a also shows the somewhat surprising result that wet melting paths, because of near-fractional melt extraction below the dry solidus, give a lower productivity at equal pressure than dryer paths in the pressure interval where dry melting operates.

[12] The behavior of trace water along the polybaric pHMELTS melting paths is shown in Figures 2b and 2c for various initial water contents at equal potential temperature. Figure 2b shows the evolution of the bulk partition coefficient for water. In the *Hirth and Kohlstedt* [1996] model (black line), as emphasized above, the partition coefficient D_{H_2O} is independent of water content, but decreases during progressive decompression melting because of the drop in pressure and because the modal abundance of pyroxenes, in which water is taken to be 5–10 times more compatible than in olivine, decreases during melting. On the other hand, in the pHMELTS model D_{H_2O} depends on water activity, such that sources with less water give lower D_{H_2O} at equal pressure and temperature. This aspect of the model provides a natural explanation for the observation of *Danyushevsky et al.* [2000] that H₂O partitions like La in depleted, water-poor MORB suites and like the more compatible element Nd in water-rich MORB suites. Figure 2c shows the bulk water contents of the residual assemblage along the same melting paths, showing the progressive drying out of the residue by extraction of water into the melt phase. As melt extraction decreases

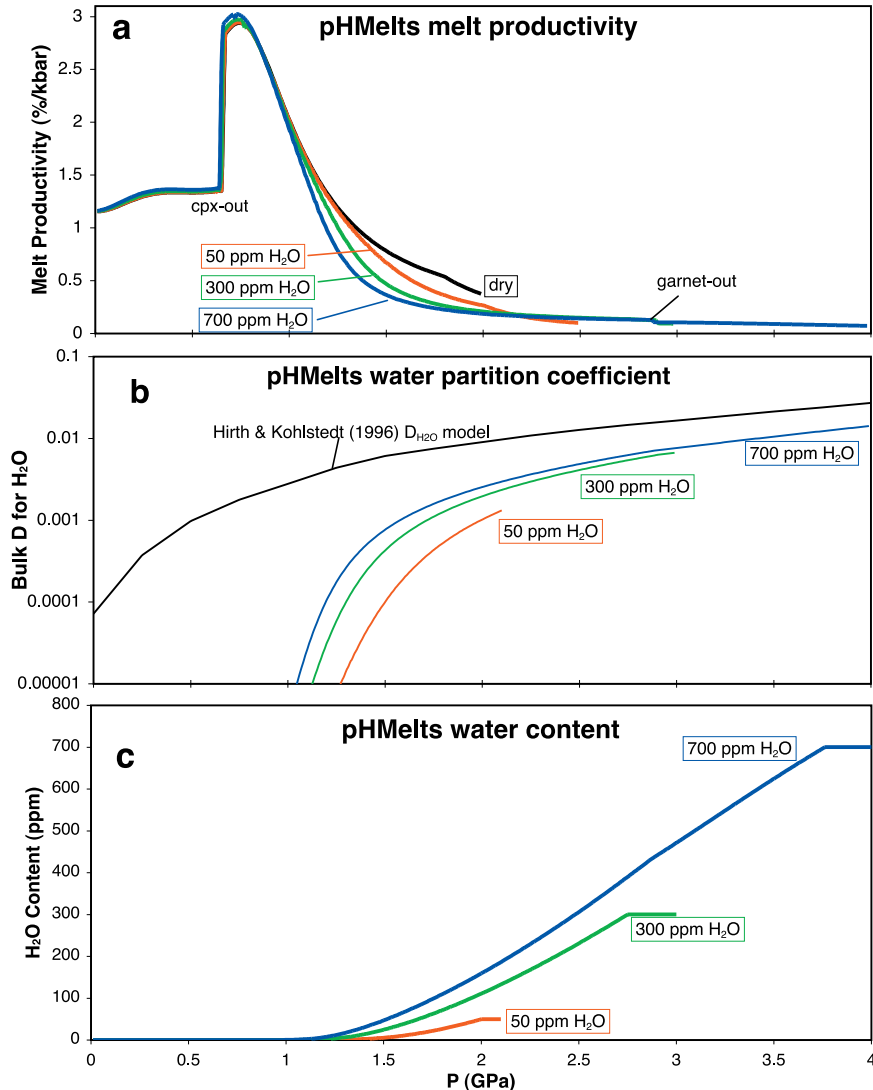


Figure 2. Melt productivity and behavior of H₂O along the melting paths shown in Figure 1. (a) Melt productivity is defined as the increase in extent of melting by mass per unit decrease in pressure, and is given in units of %/kbar. The effects of garnet and cpx exhaustion are shown. The four curves indicate the melting paths with 0, 50, 300, and 700 ppm H₂O in the source (black, red, green, and blue, respectively), all at potential temperature 1380°C. Adding water causes melting to begin at higher pressure, but the productivity of melting in this water-assisted region is much lower than that of dry melting. Furthermore, the depletion of the residue by wet melting causes the productivity of the water-bearing paths to be lower than that of the dry path even after the pressure where dry melting begins. (b) The evolution of the bulk partition coefficient for H₂O between melt and residue (D_{H_2O}) is shown for the Hirth and Kohlstedt [1996] model, where it is a function of pressure only, and for the pHMELTS model, where it depends also on water content. In pHMELTS, D_{H_2O} is lower along paths with lower initial H₂O and also decreases during melt (and water) extraction, approaching zero as residual H₂O content approaches zero. (c) The evolution of source and residue H₂O content along the 50, 300, and 700 ppm initial H₂O continuous melting paths is shown. Note that on each path the pressure where the H₂O content goes to zero (Figure 2c) is the same as the pressure where the partition coefficient becomes effectively zero (Figure 2b) and the melt productivity reaches the value of dry peridotite at the dry solidus (Figure 2a).



the H₂O content of the residue along each path, D_{H_2O} drops due to the concentration effect on partitioning in addition to the pressure and modal effects. Hence water extraction is an accelerating process, in which water approaches perfectly incompatible behavior as its abundance decreases, yielding a sharper wet-to-dry transition than would the *Hirth and Kohlstedt* [1996] model.

[13] Model primary aggregate liquids can be generated by integrating (i.e., mixing) the incremental liquids generated along the one-dimensional streamline calculated by the melting model using any of a number of formalisms that describe the net magmatic output of a melting region of given flow geometry. We found that in the Azores region the passive flow formalism [e.g., *McKenzie and Bickle*, 1988] leads to excessive weighting of high pressure liquids and hence SiO₂ too low and FeO* too high at reasonable potential temperatures. This behavior is rather insensitive to source composition since SiO₂ activity is buffered by the olivine-orthopyroxene assemblage and is hence only a strong function of pressure. This may, of course, simply reflect errors in the pMELTS model (although model SiO₂ compares well to 1 GPa experiments [*Ghiorso et al.*, 2002]), but we found that a mixing model with a component of active flow [*Scott and Stevenson*, 1989; *Forsyth*, 1992; *Spiegelman*, 1996] can match all the observables simultaneously. Hence we use here a mixing model that simulates a passive flow at depth and a transition to buoyantly driven active flow at a pressure of 0.6 GPa. Such a flow field might arise from internal buoyancy of retained melt and hence be restricted to the shallow part of the melting regime where most melt is accumulated [e.g., *Scott*, 1992, Figure 4.2b]. This flow field is simulated using the following integration scheme: melt increments produced on streamlines that exit the melting regime below 0.6 GPa are integrated up to the pressure where they exit the melting regime, whereas streamlines that cross 0.6 GPa are integrated all the way to the base of the crust. In order to emphasize as clearly as possible the effect of water addition alone, we hold the component of active flow constant in all the calculations below, although the SiO₂ and FeO* data could be better fit

by adding a transition from passive to partly active flow.

[14] The final step in the model is fractional crystallization of the primary aggregate compositions until their MgO contents reach 8%. Fractionation is modeled using MELTS at 500 bars and 1 log unit below the quartz-fayalite-magnetite buffer. At low pressure, the original MELTS calibration [*Ghiorso and Sack*, 1995] is more reliable than the newer pMELTS calibration [*Ghiorso et al.*, 2002], which is optimized for high pressure and is used here for melting calculations. MELTS accounts for the effects of H₂O in the fractionating liquid and for consistency is used both for forward-fractionating the model liquids and, in the following comparison against natural basalt glasses, for forward- or back-fractionating the measured glass compositions to a common 8% MgO.

3. Application to the Mid-Atlantic Ridge Near the Azores

[15] The development of the pHMELTS model was motivated by the desire to understand and interpret data on a suite of axial mid-ocean ridge basalt glasses from the segments of the mid-Atlantic Ridge near the Azores hotspot. The sample suite was collected by the FAZAR expedition (cruise 127, legs 1 and 2, of the Atlantis II) in 1992 and covers a latitude range from 33 to 41°N (Figure 3; segment definition and nomenclature by *Detrick et al.* [1995]). A variety of analyses of subsets of this suite have been published already: Sr, Nd, and Pb isotopes and selected trace elements by XRF and isotope dilution are in *Dosso et al.* [1999]; U-series disequilibria on samples from the Azores platform region of this collection were reported by *Bourdon et al.* [1996]; Noble gas concentrations and isotope ratios were measured by *Sarda et al.* [1999] and *Moreira et al.* [1999]; oxygen isotope compositions are reported by K. M. Cooper, J. M. Eiler, P. D. Asimow, and C. H. Langmuir (Oxygen isotope evidence for the origin of enriched mantle beneath the mid-Atlantic ridge, manuscript submitted to *Geochemistry Geophysics Geosystems*, 2003, hereinafter referred to as Cooper et al., submitted manuscript, 2003); chalcophile element data are

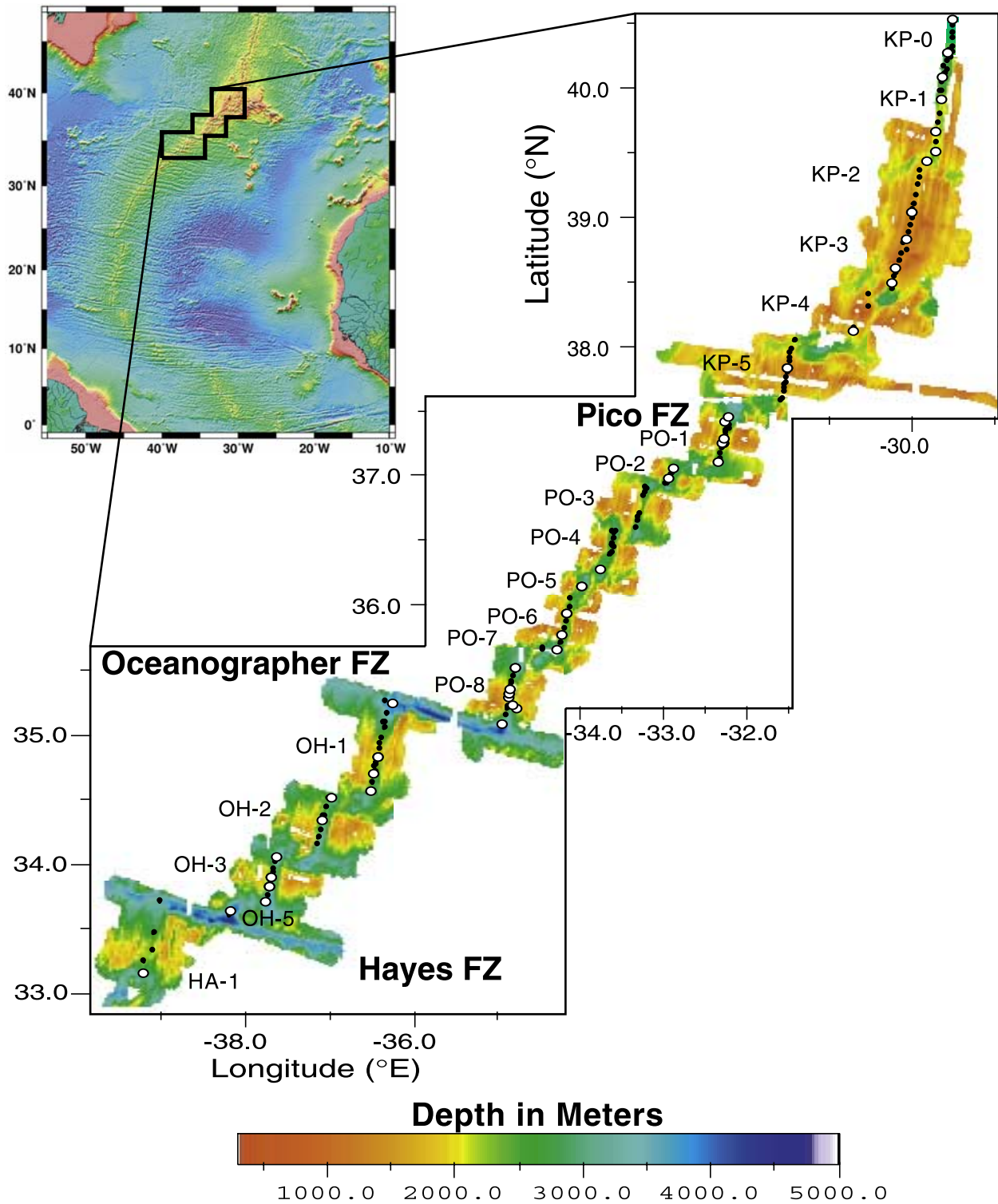


Figure 3. Sample locality map for mid-Atlantic Ridge basalt data from the FAZAR cruise (Atlantis II cruise 127, legs 1 and 2). Small black dots are all sample locations where glass was recovered; this paper focuses mostly on samples for which H₂O concentration has been measured, shown by white circles. Bathymetry along axis and segment nomenclature from *Detrick et al.* [1995]; inset is shaded relief image of satellite-based bathymetry of *Smith and Sandwell* [1997]. Segments KP-2 and KP-3 sit atop the Azores platform; the axial depth of the ridge increases both north and south from this plateau.

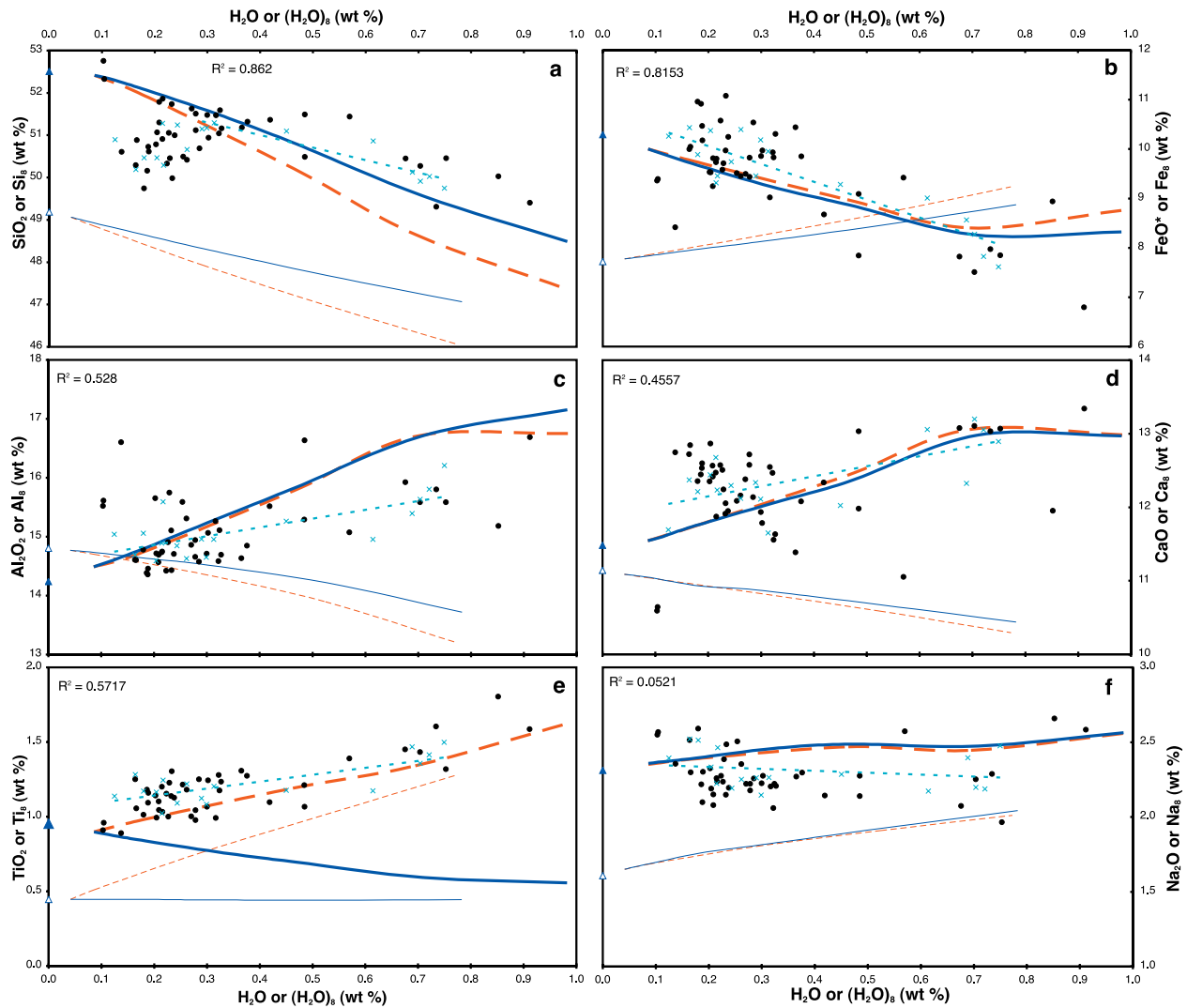


Figure 4. Major element compositions of FAZAR samples compared to the pHMELTS model as a function of H₂O content. Data for which both major elements and H₂O are measured on the same glass are shown as filled black circles; averages of all samples from a segment are plotted as cyan crosses. Data have been corrected for low-pressure fractionation to 8% MgO. A least-squares regression fit to the segment-average data of each oxide against (H₂O)₈ is shown in each panel as a cyan dotted line and the r² value of the regression is given. For Si₈, where the data increase until ~0.3% (H₂O)₈ and then decrease, the regression only includes the higher water-content data. The primary aggregate liquids (light curves) and liquids forward-fractionated to 8% MgO (heavy curves) predicted by the pHMELTS model are shown for depleted peridotite (Table 1) with 50 ppm H₂O to which is added only H₂O (solid blue curves), or TiO₂ and H₂O (long-dashed red curves). In each case the most enriched source composition shown has 700 ppm bulk H₂O. The primary liquids are generated by a mixed passive flow/active flow integration of the increments of melt produced by a polybaric, adiabatic, continuous melting path with 1% residual porosity as described in the text. The fractionated liquids are generated from these primary liquids using MELTS [Ghiorso and Sack, 1995] to evolve them to 8% MgO at low pressure. The white and filled triangles on the x axis show the compositions of primary and fractionated liquids, respectively, generated by pMELTS under the same conditions with zero H₂O.

given by Yi et al. [2000a, 2000b]; volatile concentrations and degassing corrections are given by Dixon et al. [2002]. Data have been corrected for low-pressure fractionation to 8% MgO in a way

that accounts for the heterogeneity of this suite and the effects of H₂O on fractionation [Asimow and Langmuir, 1998]; the scheme is guided by MELTS [Ghiorso and Sack, 1995] and represents an im-



provement over methods such as generic correction slopes [e.g., *Klein and Langmuir, 1987*], simple regression [e.g., *Plank and Langmuir, 1988*], universal polynomial working curves [*Niu et al., 1999*], and anhydrous calculations with limited calibration sets [*Weaver and Langmuir, 1990; Ariskin et al., 1993; Yang et al., 1996*]. Full major element and trace element results and details of fractionation correction for the entire collected suite (265 distinct glass compositions from 55 dredges and 152 wax cores) will be presented in a separate paper in this journal (Asimow et al., in preparation, 2003); in this paper we focus on testing the model of hydrous melting against the subset of 56 samples on which H₂O contents have been measured (white circles in Figure 3).

3.1. Major Elements

[16] Since our purpose here is to test the effect of H₂O on the melting and fractionation process, the model is compared to data using H₂O as the abscissa in Figure 4. Data are plotted after corrections for degassing [*Dixon et al., 2002*] and fractionation, assuming H₂O to be perfectly incompatible and undersaturated during fractionation. The notations (H₂O)₈, Si₈, Ti₈, Fe₈, etc. refer to weight percent oxides estimated for the liquid evolved from or parental to a given sample at the point where the liquid line of descent crosses 8.0% MgO. In Figure 4, small black circles are individual samples on which both major elements and water have been measured. Cyan crosses are average values of fractionation-corrected major elements for all samples from a given segment (Figure 3) on which major elements have been measured plotted versus average values of (H₂O)₈ for all samples from a given segment on which H₂O concentrations have been measured; in each segment many more samples contribute to the major-element average composition than to the average water content. Segment-average and individual-sample data show similar trends, with reduced scatter in the major element data for segment-average points. For this exercise, we exclude the North Oceanographer Fracture Zone (segment PO-8 in the nomenclature of *Detrick et al. [1995]*) samples, which have been shown to reflect an isotopically distinct and less H₂O-rich

Table 1. Fitted End-Member Source Compositions

Depleted Source	Enriched Sources ^a			
	1	2	3 (4)	
SiO ₂ (wt.%)	46.66		46.60	
TiO ₂	0.10	60	0.10 (0.29)	
Al ₂ O ₃	3.95		3.95	
Cr ₂ O ₃	0.48		0.48	
FeO	7.00		6.99	
MgO	38.36		38.31	
CaO	3.19		3.19	
Na ₂ O	0.25		0.25	
K (ppm)	7.5	350000	140000	441
P	23.5	74000	29600	115
Rb	0.02	850	340	1.07
Sr	8	22000	8800	35.3
Zr	3.2	8900	3560	14.2
Nb	0.05	1850	740	2.34
Cs	0.0003	9.4	3.76	0.0120
Ba	0.1	12200	4880	15.2
La	0.07	1150	460	1.50
Ce	0.25	2450	980	3.29
Nd	0.37	1290	516	1.97
Sm	0.17	230	92	0.455
Eu	0.086	70	28	0.173
Dy	0.39	40	16	0.439
Er	0.24	0	0	0.240
Yb	0.24	0	0	0.240
Hf	0.108	182	72.8	0.333
Ta	0.004	100	40	0.128
Pb	0.013	58	23.2	0.0849
Th	0.004	105	42	0.1341
U	0.002	30	12	0.0392
H ₂ O	50	524485	209794	700
⁸⁷ Sr/ ⁸⁶ Sr	0.7026	0.7038	0.7038	0.7035
¹⁴³ Nd/ ¹⁴⁴ Nd	0.51325	0.51285	0.51285	0.51293
²⁰⁶ Pb/ ²⁰⁴ Pb	18.00	20.00	20.00	19.69
²⁰⁷ Pb/ ²⁰⁴ Pb	15.50	15.65	15.65	15.63
²⁰⁸ Pb/ ²⁰⁴ Pb	37.65	39.50	39.50	39.22

^a Enriched sources are as follows: component 1, addition of trace elements and H₂O only, upper limit of enrichment; component 2, addition of trace elements, H₂O, and TiO₂ only; component 3, lower limit of enrichment, 0.12% of component 1 added to depleted source; component 4, 0.3% of component 2 added to depleted source, differs only in TiO₂ content from component 3.

source component than the Azores platform [*Shirey et al., 1987; Dixon et al., 2002*]. We also exclude two samples from segment KP-5 that have experienced open-system degassing and whose pre-eruptive H₂O content cannot be established with confidence. In the initial model to be tested, the enriched component consists only of water and trace elements; also, the potential temperature and flow-field are held constant. Hence this model tests what aspects of the Azores platform anomaly are attributable purely to H₂O addition rather than



thermal, dynamical or other chemical anomalies. For this purpose, K_2O and P_2O_5 are treated as trace elements and are deferred to the binary mixing calculation below.

[17] Reasonable fits to the low- H_2O end of the data require a depleted source composition, equivalent to the residue after extracting about 1% melt from the fertile lherzolite model of *Hart and Zindler* [1986]. This end member contains about 50 ppm H_2O ; its composition is shown in Table 1. We modeled the melting of this depleted source and of mixed sources with up to 700 ppm bulk H_2O ; the enriched component initially consists only of H_2O and trace elements that do not affect the melting relations. A potential temperature of $1380^\circ C$, which for this composition intersects the dry solidus at 2 GPa, was selected because it generates normal 7 km crustal thickness with 50 ppm H_2O . The $1380^\circ C$ metastable adiabat is shown in Figure 1 along with the pressure-temperature trajectories of the melting paths for the 50, 300, and 700 ppm H_2O calculations.

[18] Figure 4 shows major element composition as a function of H_2O content for primary aggregate liquids (fine solid blue lines) and liquids fractionated to 8% MgO (bold solid blue lines) generated from this range of sources. The changes in primary liquid composition are fairly small. They approximate the effects of simple increase in mean pressure of melting due to addition of deep melts from the hydrous melting region below the dry solidus: MgO and FeO* go up, other oxides go down. Where the model trends of the primary aggregate liquids and the liquids fractionated to 8% MgO are not parallel, we attribute the difference in these slopes to the effects of H_2O on the liquid line of descent. This is an aspect of the problem that, while well known to petrologists, has perhaps received less attention in modeling of mid-ocean ridge variations than it requires. H_2O in the fractionating liquids has a strong effect on the fractionation path, promoting olivine fractionation relative to plagioclase and, to a lesser extent, clinopyroxene (cpx) [*Yoder and Tilley*, 1962; *Michael and Chase*, 1987; *Sinton and Fryer*, 1987; *Danyushevsky*, 2001]. *Kushiro* [1975] provides a useful qualitative explanation of the sense

of this effect: addition of monovalent cations such as hydrogen tends to depolymerize the silicate network in the melt, which shifts liquidus boundaries so as to stabilize minerals with the most depolymerized structure. Olivine, containing isolated SiO_4 tetrahedra, is favored relative to cpx, a chain silicate, and especially relative to plagioclase, a framework silicate. The effect is proportional to the mole fraction of the cation, such that a given weight percent of H_2O has a much larger effect than a comparable weight of Na_2O or K_2O . A mid-ocean ridge basalt has the normal fractionation sequence olivine followed by olivine + plagioclase and then by olivine + plagioclase + cpx. The effect of H_2O is to delay multiple saturation to lower temperature and liquid MgO content as well as to increase the abundance of olivine in the crystallizing assemblage after multiple saturation. The manifestations of these changes are discussed oxide-by-oxide below, but the general sense is, for a given model primary aggregate liquid, to (1) reduce model Fe_8 , since Fe partitions into olivine; (2) increase model Ca_8 and Al_8 since these elements partition into cpx and plagioclase; and (3) increase model Ti_8 , Na_8 , and other incompatible elements because the increased modal abundance of the Mg-rich phase olivine in the fractionating assemblage implies a smaller mass is withdrawn from the liquid to reach 8% MgO.

[19] A notable aspect of this mechanism for modifying values of model liquid predictions at 8% MgO by water addition is that it ceases to work once multiple saturation is suppressed to less than 8% MgO, which happens at $\sim 0.7\%$ (H_2O)₈ for the present model compositions. Additional water may lower plagioclase and cpx saturation further and may affect the liquid line of descent once multiple saturation occurs, but this has no effect on the predicted value at 8% MgO.

[20] The following paragraphs compare the modeling results to the Atlantic data oxide-by-oxide and then in normative projection. We find that the model of simple H_2O addition predicts trends for all elements except Ti_8 that have the right sign of correlation versus (H_2O)₈ and that the model trends approximately parallel the principal component of



the data arrays in most elements, particularly in the most water-rich samples.

3.1.1. SiO₂

[21] The primary aggregate model liquids show a decrease in SiO₂ with increasing H₂O and the fractionated model liquids show a parallel decrease in Si₈ with increasing (H₂O)₈ (Figure 4a). We attribute this effect primarily to the pressure-dependence of SiO₂ in partial melts of peridotite and the higher mean pressure of melting induced by addition of H₂O at constant potential temperature. For samples or segments with greater than 0.3% (H₂O)₈, there is a negative correlation in the data between Si₈ and (H₂O)₈ with a slope resembling that predicted by the model. The scatter in the Si₈ data perpendicular to the modeled H₂O-addition trend are consistent with incomplete mixtures of the liquids produced in the melting regime, as is often seen when individual samples from ridge segments are considered, rather than segment averages [Klein and Langmuir, 1989]. The bulk of the data at (H₂O)₈ < 0.3% reflect a different trend, with a positive slope. This trend could be explained by an increasingly active flow regime with decreasing distance to the Azores, perhaps due to the decrease of mantle viscosity and increase in internal buoyancy of partial melts caused by increasing water in the source. Lower potential temperature in the regions farthest from the Azores would have the opposite effect of raising SiO₂ further in the most H₂O-poor samples, yielding too steep a slope in the SiO₂-H₂O diagram. Instead these data are best modeled by coupled variations in flow regime and H₂O content at approximately constant potential temperature. The flow regime effect, which seems to be most important at relatively low H₂O contents, is not included in the model trends; at higher H₂O contents, the petrologic effect of water is dominant, and the model trends appear to reproduce the high-H₂O data.

3.1.2. FeO

[22] Away from H₂O-rich hotspots like the Azores and the Galapagos [Langmuir *et al.*, 1992], there is a negative correlation between Fe₈ and axial depth attributable to the increase in mean pressure of

melting with increasing potential temperature [Klein and Langmuir, 1987]. Given the broad bathymetric high and thickened crust associated with the Azores platform, reasoning from the global trend of Klein and Langmuir would lead to the expectation of high-Fe₈ data in this region. That we find instead very low Fe₈ is surprising and requires an explanation consistent with the local observations as well as the global mid-ocean ridge data set, and this explanation is not likely to be found in any melting regime process. Indeed, the primary aggregate liquids predicted by pHMELTS show increasing FeO* with increasing H₂O, even in the absence of a temperature anomaly (Figure 4b) because of the increase in the mean pressure of melting caused by solidus depression. Rather, we may look to changes in the fractionation process to explain much of the decrease in Fe₈ with increasing H₂O in this region [Asimow and Langmuir, 2003].

[23] The effect of the change in liquid line of descent due to water addition, in FeO*-MgO space, is a lowering of Fe₈. This is seen in the model results in Figure 4b, where despite the positive slope of primary FeO* versus H₂O, a negative correlation of Fe₈ with (H₂O)₈ emerges with a slope similar to the observed Fe₈ data. Between 0.1 and 0.7 wt.% (H₂O)₈, the model primary liquids increase by ~0.75 absolute wt.% FeO*, but after fractionation the model predicts a decrease of 2 wt.% in Fe₈; this is the result of enhanced olivine fractionation. However, the most H₂O-rich model liquid does not follow the trend. Once plagioclase and cpx saturation have been suppressed to less than 8% MgO along the liquid line of descent, this mechanism no longer leads to decreases in Fe₈. In the treatment of any similar suite, it is possible to constrain the maximum magnitude of Fe₈ lowering due to the effect of H₂O on fractionation (independent of the uncertainties of a given fractionation model) given only the MgO value at which plagioclase and/or cpx saturation occurs in the driest, most depleted liquids in the suite, e.g., by examination of melt inclusions or detailed studies of phenocryst populations.

[24] The segment-averaged data show a decrease of about 3 wt.% in Fe₈ and among the individual



samples the range is as large as 4 wt.%. Hence in its present form the melting and fractionation model only explains about half the decrease in Fe_8 , but this is much better than anhydrous models that would show an increase in Fe_8 due to the increase in potential temperature needed to explain the increase in crustal thickness in this region.

3.1.3. Al_2O_3

[25] The data show, with some scatter, a positive correlation between $(\text{H}_2\text{O})_8$ and Al_8 (Figure 4c); as with the Si_8 data, the correlation is best defined by data above 0.3% $(\text{H}_2\text{O})_8$. The primary liquids predicted by the pMELTS model show a negative correlation between Al_2O_3 and H_2O , but upon fractionating to 8% MgO the model predicts a positive correlation up to 0.7% $(\text{H}_2\text{O})_8$. The model trend is steeper than that in the data; this could plausibly be related to artifacts of saturation temperature or plagioclase composition in the MELTS calculation. The increase in Al_8 in H_2O -rich model liquids is attributable to the suppression of plagioclase during fractionation, much as the decrease in Fe_8 was attributed to the complementary enhancement in olivine fractionation. That primary Al_2O_3 and fractionated Al_8 vary in opposite senses demonstrates again the importance of considering the effects of H_2O on fractionation as well as on the melting process.

3.1.4. CaO

[26] The signal-to-noise ratio in the Ca_8 data is low; CaO is the most difficult oxide to accurately correct to 8% MgO in this suite (Asimow et al., in preparation, 2003). There is no significant correlation of Ca_8 with enrichment in the individual sample data, but a positive correlation with $(\text{H}_2\text{O})_8$ can be recognized in the segment averages: the most H_2O -rich segments as a group have higher average Ca_8 than the more H_2O -poor segments (Figure 4d). There are evidently other factors affecting CaO and Ca_8 , but increase with $(\text{H}_2\text{O})_8$ does seem to be one principal component of the averaged data. As with Al_8 and Fe_8 , the model reproduces this observation despite showing the opposite trend of decreasing CaO in the primary liquids with increasing H_2O , in this case

because of the suppression of cpx fractionation by H_2O .

3.1.5. TiO_2

[27] Figure 4e shows that when only H_2O is added to the source, the model fails to reproduce the positive correlation between Ti_8 and $(\text{H}_2\text{O})_8$. TiO_2 in the primary liquids is insensitive to H_2O addition. This may result from an effect that is real, but exaggerated in pMELTS, namely the decrease in Ti concentrations in near-solidus alkali-rich liquids [Baker and Stolper, 1994; Baker et al., 1995], such that the low-melt fraction liquids created by water-enhanced deep melting do not add much Ti to the aggregate liquid. The effect of H_2O on the fractionation path, however, is evident in Ti_8 . H_2O promotes olivine fractionation relative to plagioclase and cpx; since olivine is richer in MgO than these other phases, this leads to a smaller mass of crystals being fractionated from the more H_2O -rich primary liquids to reach 8% MgO. Since TiO_2 is incompatible during fractionation of olivine, plagioclase, and/or cpx, a decrease in fractionated mass leads to decreasing Ti_8 . This is the only clear failure of the simple pMELTS model of addition of H_2O at constant potential temperature to explain a major element trend. For this reason, we also consider a model in which the enriched source consists of H_2O , trace elements, and TiO_2 . This is shown in Figure 4 by the red long-dashed lines (fine dashed red line showing primary aggregate model liquids, bold dashed red line showing model liquids fractionated to 8% MgO). The best fit is obtained if the enriched component has a $\text{TiO}_2/\text{H}_2\text{O}$ ratio of 3, in contrast to the typical MORB source with a $\text{TiO}_2/\text{H}_2\text{O}$ ratio of about 10–20. In detail, the addition of TiO_2 to the enriched component affects all the other major element trends, but none of the changes are large enough to affect the conclusions of this exercise.

3.1.6. Na_2O

[28] Consideration of Na presents an interesting puzzle because an anomaly like the Azores has several competing effects on Na_8 with opposite sense. A hotspot anomaly would be expected to lower Na_8 because Na_2O is incompatible and there

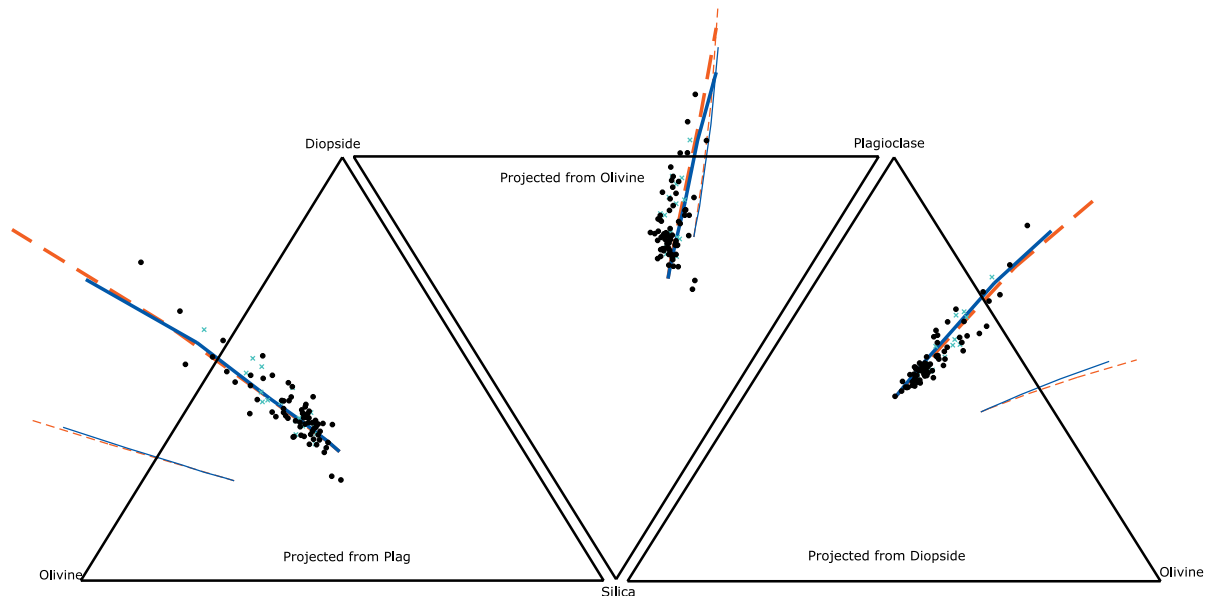


Figure 5. Projection of the FAZAR major element data and pHMELTS model liquids into the normative tetrahedron olivine-cpx-plagioclase-silica using the algorithm of *Walker et al.* [1979]. Compositions are plotted anhydrous and with all Fe as FeO. Symbols are the same as Figure 4. The decrease in normative olivine upon fractionation from the primary aggregate model liquids to 8% MgO is evident, as is the excellent match in three dimensions between the fractionated model trends and the data.

is an increase in extent of melting associated with high potential temperature or excess H₂O-driven melting. On the other hand, trace elements with bulk partition coefficients similar to that expected for Na₂O are often very high in hotspot-affected basalts because of source enrichment. Furthermore, in passive-flow melting regimes, the addition of a tail of low-degree melting at the base of the melting regime can draw in considerable extra Na and give increasing Na₂O in primary liquids despite constant source composition and increasing maximum extent of melting. However, this enhancement may be moderated by the probable increase in bulk partition coefficient for Na with increasing pressure. On yet another hand, Na is incompatible during fractionation and hence any decrease in the mass fractionated to reach 8% MgO with increasing olivine fractionation (as seen above for Ti) may cause a decrease in Na₈. In the case of our data from the Azores region, there is very little regional signature in Na₈ and even in the most H₂O-rich segment high and low-Na₈ samples co-exist (Figure 4f). In detail, there appears to be a decrease in Na₈ from the most depleted samples up to about 0.3% H₂O, followed by constant or

perhaps slightly increasing Na₈ in the water-rich part of the data. In our model, which at this stage disregards effects of potential temperature or source enrichment of Na₂O, we predict a gentle increase in primary Na₂O due to low-degree melts from deep in the melting regime, and essentially constant Na₈ up to ~0.7 wt.% H₂O due to the effects of increased olivine fractionation from these primary liquids. The data do not seem to require source enrichment in Na, although it might be required to compensate for an increase in potential temperature.

3.1.7. Major Element Summary

[29] Although the major element variations cannot be reduced to any single parameter of variation, the results of the pHMELTS model suggest a set of physical and chemical mechanisms that explain the sign and in most cases the approximate magnitude of that considerable part of the variance in the observed fractionation-corrected data (about half the total variance) accounted for by correlation with H₂O. Among Si₈, Ti₈, Al₈, Fe₈, Ca₈, and Na₈, only Ti₈ requires any direct contribution from the enriched source component. An alternative



viewpoint to these oxide-oxide variation diagrams is afforded by projection of the data and model liquid compositions into the normative tetrahedron olivine-cpx-plagioclase-silica, for example using the projection scheme of *Walker et al.* [1979]. The position of a point in this space depends on all the major oxides and so presents information in a complementary manner to the individual oxide plots. In Figure 5 the position in this tetrahedron is shown by projection onto three of the bounding triangles. The fractionation-corrected data (individual samples, black circles; segment averages, cyan crosses) as well as the primary aggregate model trends (light lines; solid blue lines for trace element and H₂O addition only, red long-dashed lines for model with Ti addition) and fractionated model trends (bold lines) are shown as in Figure 4. Viewed from all three of these angles, the projections of the fractionated model trends fit the data very well. The data and model trends are all essentially radial from the silica vertex, and project to a tight circular cluster and very short curves when viewed from the silica vertex. Figure 5 shows that pHMELTS and the particular water-addition model described here provide an excellent quantitative fit to the first principal component of major-element variation in the fractionation-corrected data.

3.2. Crustal Thickness

[30] The thickness of the oceanic crust is an essential first-order constraint on ridge melting processes and mantle temperature, and a model for variations along axis must account for the absolute value and the changes in crustal thickness as well as the chemistry of the basalts. There are, of course, uncertainties in the determination of crustal thickness by either seismic or gravity-based methods. In the study area, there are several seismic determinations of absolute crustal thickness by refraction profiling [*Fowler, 1976; Sinha and Loudon, 1983; Hooft et al., 2000*] or Rayleigh wave dispersion [*Searle, 1976*] and one gravity study that interprets variations in mantle Bouguer anomaly in terms of relative along-axis variations in crustal thickness [*Detrick et al., 1995*]. These studies show that crustal thickness is highly vari-

able at the segment-scale. There are variations along-axis, e.g., varying from 3.5 km at segment end to 8 km at segment center with a mean of 5.6 km directly along-axis on segment OH-1 [*Hooft et al., 2000*]. Variations across-axis have been interpreted at one location in terms of temporal variations, in the case of an off-axis line on 2 Ma crust parallel to OH-1 that yields 1–2 km more crust than the corresponding on-axis line [*Sinha and Loudon, 1983*]. At another location, crustal thickening from 3 km on-axis to 8 km at 10 km off-axis on the FAMOUS segment was interpreted as distributed crustal accretion [*Fowler, 1976*]. The only direct determination of crustal thickness in the Azores platform region is the Rayleigh wave study of *Searle* [1976], which reports 8.0 ± 0.6 km for the center of the platform and 6.3 km for the flanks of the platform near FAMOUS (i.e., segment PO-3) or segment KP-0. Given the spatial complexity and disagreement among various studies, it is difficult to unambiguously extract an along-axis gradient in segment-average crustal thickness from the seismic measurements. Indeed, values near 8 km have been reported throughout the study area. However, a reasonable interpretation suggests total thickening of ~ 3 km over the whole study area, with about 1.5 km between FAMOUS at 37°N and KP-3 at 39°N. This is consistent with the gravity interpretation of *Detrick et al.* [1995] who obtain a maximum increase in crustal thickness by attributing all mantle Bouguer anomalies to Airy isostasy, ignoring potential mantle or crustal density variations. Their result is an increase of 3.5–4 km over the whole study area, of which 2–3 km occurs between FAMOUS and the Azores platform.

[31] Estimates of segment mean crustal thickness can be compared to the results of two-dimensional melting models, since both are meant to be determinations of total magma budget and are insensitive to segment-scale along-axis flow of mantle or melt. In several models of anhydrous melting and passive-flow mixing at mid-ocean ridges, a thickening of the crust by 4 km, from 7 km to 11 km, requires an increase of at least 75°C in potential temperature [*Kinzler and Grove, 1992; Langmuir et al., 1992; Asimow et al., 2001*]. The model of *McKenzie and Bickle*

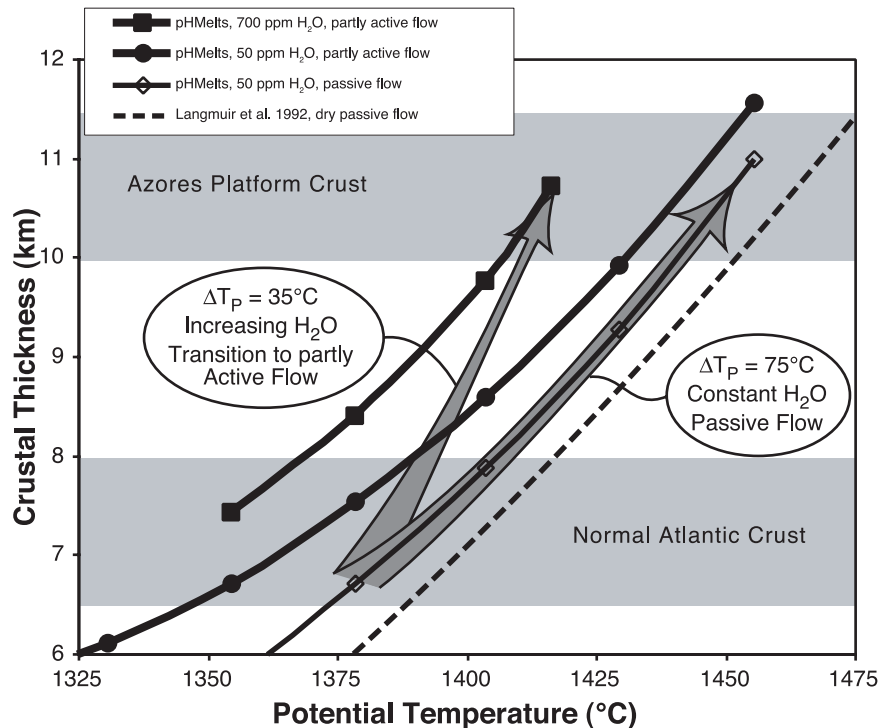


Figure 6. Crustal thickness versus potential temperature showing the changes in potential temperature needed to achieve an increase of 3–4 km in crustal thickness from typical Atlantic values near 7 km to Azores platform values of 10–11 km [Detrick *et al.*, 1995]. Passive-flow melting regimes with constant H₂O contents require an increase of $\geq 75^{\circ}\text{C}$ in potential temperature to increase crustal thickness this much (right arrow), whether estimated from the pHMELTS model or the anhydrous model of Langmuir *et al.* [1992]. Such models fail to fit the major-element composition data in this region. On the other hand, an increase of 1 km in crustal thickness results solely from the addition of the quantity of H₂O required by the measured H₂O in the basalts. A further 1 km increase results from a transition to partly active flow (required to explain the high SiO₂ and low FeO* of the moderately enriched samples in the present data suite). With an increase of only 35°C in potential temperature, a coupled trend of increased temperature, increased H₂O, and increasingly active flow (left arrow) explains the full crustal thickness anomaly of 3–4 km.

[1988], which has a near-solidus productivity much too high for volatile-affected melting, requires an increase of 50°C in potential temperature to reach crustal thickness 3 km above average. The effect of water addition on oceanic crustal thickness and the corresponding relationship between crustal thickness and potential temperature has previously been modeled only by Robinson *et al.* [2001] using an extension of McKenzie and Bickle's [1988] parameterization.

[32] The behavior of crustal thickness as a function of potential temperature and source H₂O content in the pHMELTS calculations is shown in Figure 6. A variation from 50 ppm to 700 ppm H₂O in the source at a constant potential temperature of

1380°C yields an increase in crustal thickness of ~1 km, from 7.5 to 8.4 km. That is, the model predicts an increase of 1 km in crustal thickness in the absence of any thermal anomaly, purely as a result of the enhancement of melting by the addition of water. If the flow field undergoes a transition to an increasingly active regime with approach to the Azores platform, as we argued above to explain the SiO₂ data, this will add a further 1 km of crustal thickness at constant potential temperature. In combination with these two effects, an increase of only 35°C in potential temperature, to 1415°C, yields a total increase of ~4 km in crustal thickness. Notably, the effects of potential temperature and water addition reinforce each other. That is, a given amount of water has a noticeably larger

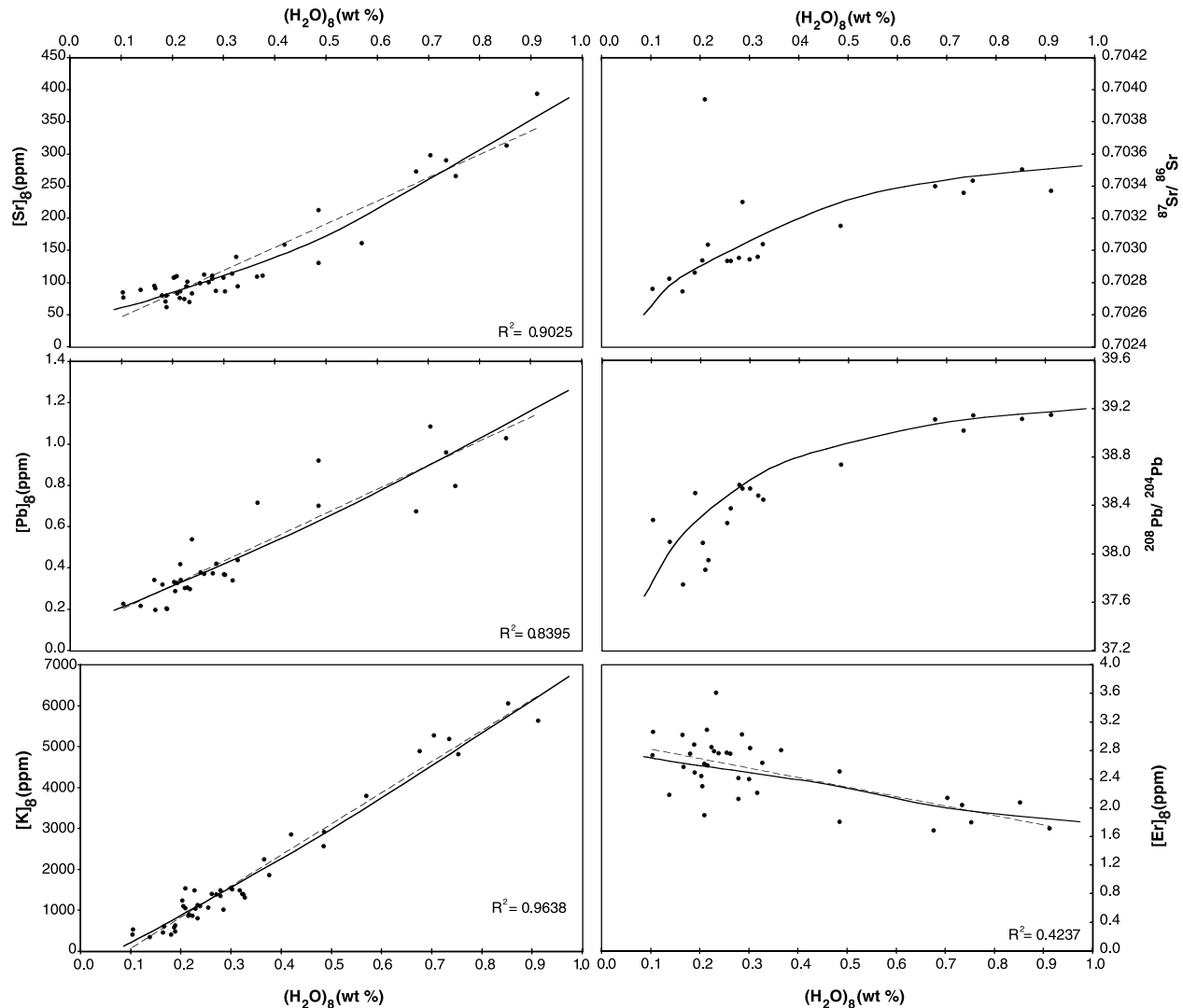


Figure 7. Representative fractionation-corrected trace element and radiogenic isotope data versus H_2O content [also corrected for degassing, *Dixon et al.*, 2002] are compared to the results of a model of binary mixing of sources coupled to the pHMELTS melting and fractionation models. Most elemental concentrations are consistent with binary linear mixing in this space, so depleted and enriched components were fitted to produce a mixing trend approximating the regression line through the data. The fitted source compositions are shown in Table 1 and plotted in Figure 8. Curvature in the elemental Sr model results from partitioning of Sr into plagioclase during fractionation. All the incompatible trace elements (Cs, Rb, Ba, Th, U, Nb, Ta, La, Ce, and Zr) produce plots similar to the K plot, with linear correlations $r^2 \geq 0.85$. The model mixing trend for Er (Yb is similar) has a concentration of zero in the enriched end member. The outlying point in $^{87}\text{Sr}/^{86}\text{Sr}$ versus $(\text{H}_2\text{O})_8$ space is considered to be contaminated by seawater Sr; it also plots far from the $^{87}\text{Sr}/^{86}\text{Sr}$ versus ϵ_{Nd} correlation defined by the rest of the data.

effect at modestly higher potential temperature, e.g., 1 km at 1380°C and 1.5 km at 1415°C . Conversely, in the presence of water a much smaller temperature anomaly yields the maximum increase in crustal thickness inferred by seismic and gravity methods. We emphasize that the 75°C increase in potential temperature required by an

hydrous models to explain the increased crustal thickness at the Azores would lead to major increase in Fe_8 , precisely the opposite of what is observed. Although the pHMELTS model has many shortcomings and contains assumptions that cannot be defended in great detail, it shows that the addition of H_2O to the source, together with a small

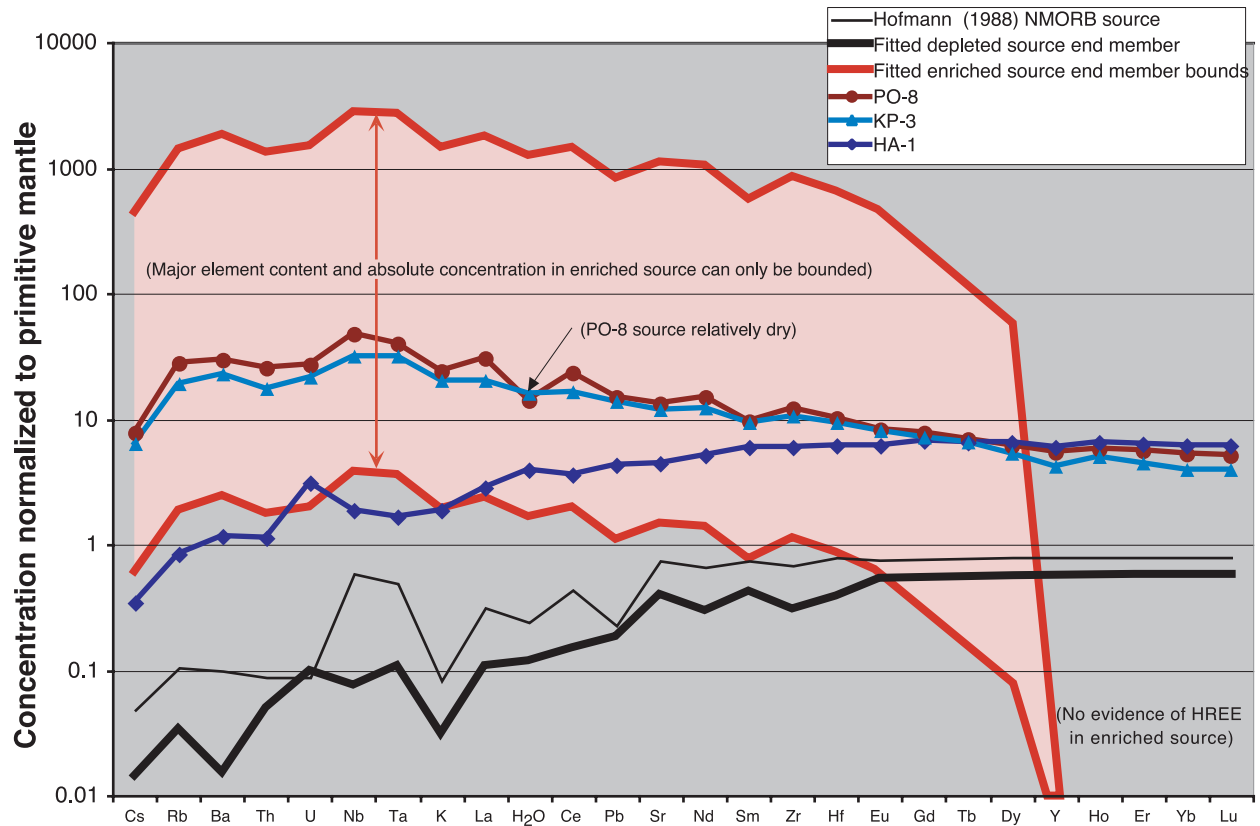


Figure 8. Primitive-mantle normalized segment-average trace element data for the most depleted and most enriched segments in this study are compared to the model depleted and enriched source compositions (Table 1). Since the fitting procedure is unable to resolve major elements or trace elements more compatible than Dy in the enriched source, its absolute position is arbitrary, and can plot anywhere between the upper and lower limit curves shown. The depleted model source is significantly more depleted than average NMORB source models, e.g., that of *Hofmann* [1988].

temperature anomaly, can explain geophysical as well as petrological observations.

3.3. Trace Elements and Isotopes

[33] When radiogenic isotope ratios and fractionation-corrected trace element concentrations are plotted against fractionation-corrected bulk H₂O contents for the subset of samples where all these indicators have been analyzed, as in Figure 7, the results appear consistent with binary mixing. Hence we have inverted for the composition of two source components. The fitting utilizes the pHMELTS model liquids at 8% MgO; however, the adjustable quantities are not erupted compositions but source compositions. Hence this exercise accounts for all the effects of water addition on melting and fractionation. This is significant because the incompat-

ible elements are significantly more enriched in model liquids derived from melting regimes richer in H₂O due to the large volume of deep mantle that experiences small degrees of hydrous melting. Ignoring this effect would lead to an overestimate by about a factor of two in the abundances of the most incompatible elements in the enriched component. The quality of the resulting fits can be seen in Figure 7 for several representative trace elements and isotope ratios. Because the variations in partition coefficients during melting and fractionation are small for most of these elements, the model mixing trends for most trace elements are essentially linear. However, participation of plagioclase in the fractionation process leads to significant curvature in the array of fractionated liquids from mixed sources for Sr, and this is arguably more consistent with the data array than simple mixing of liquids.



Because the enriched end member has higher concentrations of Sr, Nd, and Pb than the depleted end member, the same model predicts concave-downward hyperbolic mixing trends that fit the data very well in radiogenic isotope ratios versus H₂O (Figure 7). In isotope ratio-ratio plots (not shown), the model trends have a slight curvature, but the data array could be fitted equally well with straight lines. In other words, isotope ratio-ratio plots do not in this data set resolve differences in Sr/Nd, Sr/Pb, or Nd/Pb ratios among the end members. For elements more compatible than Dy, the best fit is obtained with a concentration of zero in the enriched end member, but this result should simply be taken to imply that given the small mass fraction of the enriched component, its composition is not sufficiently enriched in these elements to have a significant impact on the composition of the mixed sources.

[34] The fitted end-member compositions chosen are given in Table 1 and plotted in Figure 8. Because the trace element plus H₂O content of the enriched component is normalized to 100% (that is, unresolved major elements are excluded), this exercise gives the upper limit on the water content and degree of enrichment of this source and a lower limit on the mass fraction added. The Ti-free model end member is 52 wt.% H₂O, has primitive-mantle normalized incompatible element abundances of about 1000–2000, and only 0.13% by mass of this component is required to generate the most enriched samples. The Ti-bearing model (with TiO₂/H₂O ratio of 3) dilutes these numbers to 20 wt.% H₂O, incompatible concentrations of 500–700 times primitive, and 0.3% added to the most enriched source mixture. We consider these water-dominated compositions for the enriched component unlikely because H₂O/Ce ratios in the water-rich samples are consistent with magmatic partitioning rather than involvement of hydrous fluids [Dixon *et al.*, 2002]; however, if the enriched component is a silicate melt, then it must contain major elements that are not resolved by our fitting. The whole abundance pattern of the enriched component will be moved downward by the presence of major elements that are unresolved because the mass fraction of the enriched source is so small.

The lower limit is obtained by assuming that the most enriched sample derives from melting the enriched component in pure form, in which case the enriched component would be of peridotite bulk composition with 700 ppm H₂O and have primitive-mantle normalized concentrations of highly incompatible elements near 2–3; the lower-limit enriched compositions in Table 1 are obtained by mixing the depleted source with the necessary mass fractions of the upper-limit enriched compositions so as to yield 700 ppm H₂O.

[35] On a primitive-mantle normalized diagram with the elements ordered according to the normal sequence of incompatibility in MORB [Hofmann, 1988], the pattern for the enriched source component (Figure 8) mirrors the compositions of the most enriched samples, and is fairly smooth. Anomalies are all less than a factor of two. One notable aspect of the pattern is the elevated Ce/Pb ratio (relative to primitive mantle) of the enriched component, reflecting the high Ce/Pb ratio of several of the most H₂O-rich samples (these samples also show anomalous oxygen isotope ratios (Cooper *et al.*, submitted manuscript, 2003)). The negative anomaly in Pb, a slight negative anomaly in H₂O, and positive anomalies in Nb and Ta are all features complementary to the patterns observed in subduction-related magmas [Pearce and Cann, 1973; Miller *et al.*, 1994]. In arc magmas, the complementary anomalies in these elements are normally explained by preferential extraction of fluid-mobile elements from the subducting slab to the source area in the mantle wedge. Hence the pattern observed here is consistent with recycled material residual after extraction of fluid-mobile components. However, except for compositions near the lower limit for the enriched source, this source is too enriched in incompatible elements to be recycled NMORB even without depletion during partial dehydration. Thus it seems necessary that at some stage in its evolution the enriched component was mobilized as a small-degree melt, perhaps deep in a subduction system: after dehydration and deep enough that the region metasomatized by the enriched component escaped incorporation in the subduction melting environment. It is possible that this component may have



resided for some part of its history in the continental lithosphere [McKenzie and O'Nions, 1995; Moreira and Allègre, 1999]. The present model does not account for the heterogeneities observed in this region in noble gas isotope ratios; although the elements examined here do not seem to require a third component, they do not by any means exclude it.

4. Conclusions

[36] We have developed a model for mid-ocean ridge melting regimes with small amounts of water in the source by combining the pMELTS [Ghiorso *et al.*, 2002] description of water-bearing crystal-melt phase equilibria and energetics with the formulation of solubility of water in nominally anhydrous mantle minerals described by Hirth and Kohlstedt [1996]. We use this model to investigate the major element, trace element, isotopic, and crustal thickness relations observed along the Mid-Atlantic Ridge in the vicinity of the Azores platform. In contrast to the results of standard models of anhydrous, passive-flow mid-ocean ridge basalt production, which require a $\geq 75^\circ\text{C}$ increase in potential temperature to explain the crustal thickness anomaly and fail to explain any of the trace, major, volatile, or isotopic chemical indicators, we find that a temperature anomaly of $< 35^\circ\text{C}$ and a small component of active flow together with the effects of addition of up to 700 ppm H_2O in a trace element enriched source can explain all these data to some extent. There remain features of the major-element data, including the magnitude of the overall decrease in Fe_8 and the Si_8 , Ca_8 , and Na_8 trends in the water-poor subset of the data, that are not well explained, both because of shortcomings in the quantitative petrological models and because of physical effects not yet accounted for. For many elements, notably Fe, Al, and Ca, the changes in erupted compositions are dominated by the effect of H_2O on the low-pressure fractionation path rather than any effect on primary liquid composition in the melting process. In the context of this melting and fractionation model we find that the trace element and isotopic data are well-explained by a binary mixing model in which the enriched source, though we can only

bound its absolute enrichment level, is consistent with mantle wedge peridotite that was metasomatized by a small-degree melt of a partially dehydrated subducted slab.

Acknowledgments

[37] PDA thanks Mark Ghiorso for allowing his code to be so mercilessly hacked. PDA was supported for part of this work by a postdoctoral fellowship from Lamont-Doherty Earth Observatory and later by the National Science Foundation (OCE 00-95294). CHL and JED acknowledge support by multiple grants from NSF over a period of years. This is Division of Geological and Planetary Sciences contribution number 8913.

References

- Ariskin, A. A., M. Y. Frenkel, G. S. Barmina, and R. L. Nielsen (1993), Comagmat: A FORTRAN program to model magma differentiation processes, *Comp. Geosci.*, *19*, 1155–1170.
- Asimow, P. D., and M. S. Ghiorso (1998), Algorithmic modifications extending MELTS to calculate subsolidus phase relations, *Am. Mineral.*, *83*, 1127–1132.
- Asimow, P. D., and C. H. Langmuir (1998), Segment-scale and regional systematics from 33°N to 41°N on the Mid-Atlantic Ridge: Results from the FAZAR Cruise, *Eos Trans. AGU*, *79*(46), Fall Meet. Suppl., F938–F939.
- Asimow, P. D., and C. H. Langmuir (2003), The importance of water to oceanic mantle melting regimes, *Nature*, *421*, 815–820.
- Asimow, P. D., M. M. Hirschmann, M. S. Ghiorso, M. J. O'Hara, and E. M. Stolper (1995), The effect of pressure-induced solid-solid phase transitions on decompression melting of the mantle, *Geochim. Cosmochim. Acta*, *59*, 4489–4506.
- Asimow, P. D., M. M. Hirschmann, and E. M. Stolper (1997), An analysis of variations in isentropic melt productivity, *Philos. Trans. R. Soc. London Ser. A*, *355*, 255–281.
- Asimow, P. D., M. M. Hirschmann, and E. M. Stolper (2001), Calculation of peridotite partial melting from thermodynamic models of minerals and melts. IV. Adiabatic decompression and the composition and mean properties of mid-ocean ridge basalts, *J. Petrol.*, *42*, 963–998.
- Bai, Q., and D. L. Kohlstedt (1992), Substantial hydrogen solubility in olivine and implications for water storage in the mantle, *Nature*, *357*, 672–674.
- Baker, M. B., and E. M. Stolper (1994), Determining the composition of high-pressure mantle melts using diamond aggregates, *Geochim. Cosmochim. Acta*, *58*, 2811–2827.
- Baker, M. B., M. M. Hirschmann, M. S. Ghiorso, and E. M. Stolper (1995), Compositions of near-solidus peridotite melts from experiments and thermodynamic calculations, *Nature*, *375*, 308–311.
- Bell, D. R., and G. R. Rossman (1992), Water in the Earth's mantle: The role of nominally anhydrous minerals, *Science*, *255*, 1391–1397.



- Bonatti, E. (1971), Ancient continental mantle beneath oceanic ridges, *J. Geophys. Res.*, *76*, 3825–3831.
- Bonatti, E. (1990), Not so hot “hot spots” in the oceanic mantle, *Science*, *250*, 107–111.
- Bourdon, B., C. H. Langmuir, and A. Zindler (1996), Ridge-hotspot interaction along the Mid-Atlantic Ridge between 37°30' and 40°30'N: The U-Th disequilibrium evidence, *Earth Planet. Sci. Lett.*, *142*, 175–189.
- Danyushevsky, L. V. (2001), The effect of small amount of H₂O on crystallisation of mid-ocean ridge and backarc basic magmas, *J. Volcanol. Geotherm. Res.*, *110*, 265–280.
- Danyushevsky, L. V., S. M. Eggins, T. J. Falloon, and D. M. Christie (2000), H₂O abundance in depleted to moderately enriched mid-ocean ridge magmas; Part I: Incompatible behaviour, implications for mantle storage, and origin of regional variations, *J. Petrol.*, *41*, 1329–1364.
- Detrick, R. S., H. D. Needham, and V. Renard (1995), Gravity anomalies and crustal thickness variations along the Mid-Atlantic Ridge between 33°N and 40°N, *J. Geophys. Res.*, *100*, 3767–3787.
- Dickey, J. S., Jr., F. A. Frey, S. Hart, E. B. Watson, and G. Thompson (1977), Geochemistry and petrology of dredged basalts from the Bouvet triple junction, South Atlantic, *Geochim. Cosmochim. Acta*, *41*, 1105–1118.
- Dixon, J. E., L. Leist, C. H. Langmuir, and J.-G. Schilling (2002), Recycled dehydrated lithosphere observed in plume-influenced mid-ocean-ridge basalt, *Nature*, *420*, 385–389.
- Dosso, L., H. Bougault, C. H. Langmuir, C. Bollinger, O. Bonnier, and J. Etoubleau (1999), The age and distribution of mantle heterogeneity along the Mid-Atlantic Ridge (31–41°N), *Earth Planet. Sci. Lett.*, *170*, 269–286.
- Douglass, J., J.-G. Schilling, and R. H. Kingsley (1995), Influence of the discovery and Shona mantle plumes on the southern Mid-Atlantic Ridge: Rare-earth evidence, *Geophys. Res. Lett.*, *22*, 2893–2896.
- Douglass, J., J.-G. Schilling, and D. Fontignie (1999), Plume-ridge interactions of the Discovery and Shona mantle plumes with the southern mid-Atlantic ridge (40°–55°S), *J. Geophys. Res.*, *104*, 2941–2962.
- Falloon, T. J., and L. V. Danyushevsky (2000), Melting of refractory mantle at 1.5, 2 and 2.5 GPa under anhydrous and H₂O-undersaturated conditions: Implications for the petrogenesis of high-Ca boninites and the influence of subduction components on mantle melting, *J. Petrol.*, *41*, 257–283.
- Forsyth, D. W. (1992), Geophysical constraints on mantle flow and melt generation beneath mid-ocean ridges, in *Mantle Flow and Melt Generation at Mid-Ocean Ridges*, *Geophys. Monogr. Ser.*, vol. 71, edited by J. P. Morgan, D. K. Blackman, and J. M. Sinton, pp. 1–66, AGU, Washington, D.C.
- Fowler, C. M. R. (1976), Crustal structure of the Mid-Atlantic ridge crest at 37°N, *Geophys. J. R. Astron. Soc.*, *47*, 459–491.
- Gaetani, G. A., and T. L. Grove (1998), The influence of water on melting of mantle peridotite, *Contrib. Mineral. Petrol.*, *131*, 323–346.
- Ghiorso, M. S. (1985), Chemical Mass transfer in magmatic processes: I. Thermodynamic relations and numerical algorithms, *Contrib. Mineral. Petrol.*, *90*, 107–120.
- Ghiorso, M. S. (1994), Algorithms for the estimation of phase stability in heterogeneous thermodynamic systems, *Geochim. Cosmochim. Acta*, *58*, 5489–5501.
- Ghiorso, M. S., and R. O. Sack (1995), Chemical mass transfer in magmatic processes IV. A revised and internally consistent thermodynamic model for the interpolation and extrapolation of liquid-solid equilibria in magmatic systems at elevated temperatures and pressures, *Contrib. Mineral. Petrol.*, *119*, 197–212.
- Ghiorso, M. S., M. M. Hirschmann, P. W. Reiners, and V. C. Kress III (2002), The pMELTS: A revision of MELTS for improved calculation of phase relations and major element partitioning related to partial melting of the mantle to 3 GPa, *Geochem. Geophys. Geosyst.*, *3*(5), 1030, doi:10.1029/2001GC000217.
- Green, D. H. (1973), Experimental studies on a model upper mantle composition at high pressure under water-saturated and water-undersaturated conditions, *Earth Planet. Sci. Lett.*, *19*, 37–53.
- Green, D. H. (1976), Experimental testing of “equilibrium” partial melting of peridotite under water-saturated, high-pressure conditions, *Can. Mineral.*, *14*, 255–268.
- Haar, L., J. S. Gallagher, and G. S. Kell (1984), *NBS/NRC Steam Tables*, Hemisphere Publ., Washington, D.C.
- Hanan, B. B., R. H. Kingsley, and J.-G. Schilling (1986), Pb isotope evidence in the South-Atlantic for migrating ridge hotspot interactions, *Nature*, *322*, 137–144.
- Hart, S. R., and A. Zindler (1986), In search of a bulk-earth composition, *Chem. Geol.*, *57*, 247–267.
- Hart, S. R., J.-G. Schilling, and J. L. Powell (1973), Basalts from Iceland and along the Reykjanes Ridge: Sr isotope geochemistry, *Nature Phys. Sci.*, *246*, 104–107.
- Hirose, K., and T. Kawamoto (1995), Hydrous partial melting of lherzolite at 1 GPa: The effect of H₂O on the genesis of basaltic magmas, *Earth Planet. Sci. Lett.*, *133*, 463–473.
- Hirth, G., and D. L. Kohlstedt (1996), Water in the oceanic upper mantle: Implications for rheology, melt extraction and the evolution of the lithosphere, *Earth Planet. Sci. Lett.*, *144*(1–2), 93–108.
- Hofmann, A. W. (1988), Chemical differentiation of the Earth: The relationship between mantle, continental crust, and oceanic crust, *Earth Planet. Sci. Lett.*, *90*, 297–314.
- Hofmann, A. W., and W. M. White (1982), Mantle plumes from ancient oceanic crust, *Earth Planet. Sci. Lett.*, *57*, 421–436.
- Hooft, E. E. E., R. S. Detrick, D. R. Toomey, J. A. Collins, and J. Lin (2000), Crustal thickness and structure along three contrasting spreading segments of the Mid-Atlantic Ridge, 33.5°N–35°N, *J. Geophys. Res.*, *105*, 8205–8226.
- Humphris, S. E., G. Thompson, J.-G. Schilling, and R. H. Kingsley (1985), Petrological and Geochemical Variations Along the Mid-Atlantic Ridge Between 46°S and 32°S -



- Influence of the Tristan Da Cunha Mantle Plume, *Geochim. Cosmochim. Acta*, *49*, 1445–1464.
- Karato, S.-I., and H. Jung (1998), Water, partial melting and the origin of the seismic low velocity and high attenuation zone in the upper mantle, *Earth Planet. Sci. Lett.*, *157*, 193–207.
- Kinzler, R. J. (1997), Melting of mantle peridotite at pressures approaching the spinel to garnet transition: Application to mid-ocean ridge basalt petrogenesis, *J. Geophys. Res.*, *102*, 853–874.
- Kinzler, R. J., and T. L. Grove (1992), Primary magmas of mid-ocean ridge basalts: 2. Applications, *J. Geophys. Res.*, *97*, 6907–6926.
- Klein, E. M., and C. H. Langmuir (1987), Global correlations of ocean ridge basalt chemistry with axial depth and crustal thickness, *J. Geophys. Res.*, *92*, 8089–8115.
- Klein, E. M., and C. H. Langmuir (1989), Local versus global variations in ocean ridge basalt composition: A reply, *J. Geophys. Res.*, *94*, 4241–4252.
- Kurz, M. D., W. J. Jenkins, J.-G. Schilling, and S. R. Hart (1982), Helium isotope variations in the mantle beneath the central North Atlantic Ocean, *Earth Planet. Sci. Lett.*, *58*, 1–14.
- Kushiro, I. (1972), Effect of water on the composition of magmas formed at high pressures, *J. Petrol.*, *13*, 311–334.
- Kushiro, I. (1975), Nature of Silicate Melt and Its Significance in Magma Genesis - Regularities in Shift of Liquidus Boundaries Involving Olivine, Pyroxene, and Silica Minerals, *Am. J. Sci.*, *275*, 411–431.
- Langmuir, C. H., E. M. Klein, and T. Plank (1992), Petrological systematics of mid-ocean ridge basalts: Constraints on melt generation beneath ocean ridges, in *Mantle Flow and Melt Generation at Mid-Ocean Ridges*, *Geophys. Monogr. Ser.*, vol. 71, edited by J. P. Morgan, D. K. Blackman, and J. M. Sinton, pp. 183–280, AGU, Washington, D.C.
- LeRoex, A. P., H. J. B. Dick, L. Gulen, A. M. Reid, and A. J. Erlank (1987), Local and Regional Heterogeneity in Morb From the Mid-Atlantic Ridge Between 54.5°S and 51°S - Evidence For Geochemical Enrichment, *Geochim. Cosmochim. Acta*, *51*, 541–555.
- McKenzie, D., and M. J. Bickle (1988), The volume and composition of melt generated by extension of the lithosphere, *J. Petrol.*, *29*, 625–679.
- McKenzie, D., and R. K. O’Nions (1983), Mantle reservoirs and ocean island basalts, *Nature*, *301*, 229–231.
- McKenzie, D., and R. K. O’Nions (1995), The source regions of ocean island basalts, *J. Petrol.*, *36*, 133–159.
- MELT Seismic Team (1998), Imaging the deep seismic structure beneath a Mid-Ocean Ridge: The MELT experiment, *Science*, *280*, 1215–1218.
- Michael, P. J., and R. L. Chase (1987), The influence of primary magma composition, H₂O and pressure on Mid-Ocean Ridge basalt differentiation, *Contrib. Mineral. Petrol.*, *96*, 245–263.
- Miller, D. M., S. L. Goldstein, and C. H. Langmuir (1994), Ce/Pb and Pb-isotope ratios in arc magmas and the enrichment of Pb in the continents, *Nature*, *368*, 514–520.
- Moreira, M., and C.-J. Allègre (1999), Rare gas systematics on Mid-Atlantic Ridge (37–40°N), *Earth Planet. Sci. Lett.*, *198*, 401–416.
- Niu, Y., and R. Batiza (1991), An empirical method for calculating melt compositions produced beneath mid-ocean ridges: Application to axis and off-axis (seamounts) melting, *J. Geophys. Res.*, *96*, 21,753–21,777.
- Niu, Y., K. D. Collerson, R. Batiza, J. I. Wendt, and M. Regelous (1999), Origin of enriched-type mid-ocean ridge basalt at ridges far from mantle plumes: The East Pacific Rise at 11°20’N, *J. Geophys. Res.*, *104*, 7067–7087.
- Pearce, J. A., and J. R. Cann (1973), Tectonic setting of basic volcanic rocks determined using trace element analyses, *Earth Planet. Sci. Lett.*, *19*, 290–300.
- Pitzer, K. S., and S. M. Sterner (1994), Equations of state valid continuously from zero to extreme pressures for H₂O and CO₂, *J. Chem. Phys.*, *101*, 3111–3116.
- Plank, T., and C. H. Langmuir (1988), An evaluation of the global variations in the major element chemistry of arc basalts, *Earth Planet. Sci. Lett.*, *90*, 349–370.
- Robinson, C. J., M. J. Bickle, T. A. Minshull, R. S. White, and A. R. L. Nichols (2001), Low degree melting under the Southwest Indian Ridge: The roles of mantle temperature, conductive cooling and wet melting, *Earth Planet. Sci. Lett.*, *188*, 383–398.
- Sarda, P., M. Moreira, and T. Staudacher (1999), Argon-lead isotopic correlation in Mid-Atlantic Ridge basalts, *Science*, *283*, 666–668.
- Schilling, J.-G. (1975), Azores mantle blob: The rare earth evidence, *Earth Planet. Sci. Lett.*, *24*, 103–105.
- Schilling, J.-G., M. Zajac, R. Evans, T. Johnston, W. White, J. D. Devine, and R. Kingsley (1983), Petrologic and geochemical variations along the Mid-Atlantic Ridge from 29°N to 73°N, *Am. J. Sci.*, *283*, 510–586.
- Schilling, J.-G., B. B. Hanan, B. McCully, R. H. Kingsley, and D. Fontignie (1994), Influence of the Sierra-Leone Mantle Plume On the Equatorial Mid-Atlantic Ridge: A Nd-Sr-Pb Isotopic Study, *J. Geophys. Res.*, *99*, 12,005–12,028.
- Schilling, J.-G., R. Kingsley, D. Fontignie, R. Poreda, and S. Xue (1999), Dispersion of the Jan Mayen and Iceland mantle plumes in the Arctic: A He-Pb-Nd-Sr isotope tracer study of basalts from the Kolbeinsey, Mohns, and Knipovich Ridges, *J. Geophys. Res.*, *104*, 10,543–10,569.
- Scott, D. R. (1992), Small-scale convection and mantle melting beneath mid-ocean ridges, in *Mantle Flow and Melt Generation at Mid-Ocean Ridges*, *Geophys. Monogr. Ser.*, vol. 71, edited by J. P. Morgan, D. K. Blackman, and J. M. Sinton, pp. 327–352, AGU, Washington, D.C.
- Scott, D. R., and D. J. Stevenson (1989), A self-consistent model of melting, magma migration and buoyancy-driven circulation beneath mid-ocean ridges, *J. Geophys. Res.*, *94*, 2973–2988.
- Searle, R. C. (1976), Lithospheric structure of the Azores Plateau from Rayleigh-wave dispersion, *Geophys. J. R. Astron. Soc.*, *44*, 537–546.
- Shirey, S. B., J. F. Bender, and C. H. Langmuir (1987), Three-component isotopic heterogeneity near the Oceanographer transform, Mid-Atlantic Ridge, *Nature*, *325*, 217–223.



- Sinha, M. C., and K. E. Loudon (1983), The Oceanographer fracture zone-1. Crustal structure from seismic refraction studies, *Geophysical J. Royal Astronomical Society*, *75*, 715–736.
- Sinton, J. M., and P. Fryer (1987), Mariana trough lavas from 18°N: Implications for the origin of back-arc basalts, *J. Geophys. Res.*, *92*, 12,782–12,802.
- Smith, W. H. F., and D. T. Sandwell (1997), Global seafloor topography from satellite altimetry and ship depth soundings, *Science*, *277*, 1957–1962.
- Spiegelman, M. (1996), Geochemical consequences of melt transport in 2-D: The sensitivity of trace elements to mantle dynamics, *Earth Planet. Sci. Lett.*, *139*, 115–132.
- Stolper, E. M., and S. Newman (1994), The role of water in the petrogenesis of Mariana trough magmas, *Earth Planet. Sci. Lett.*, *121*, 293–325.
- Walker, D., T. Shibata, and S. E. DeLong (1979), Abyssal tholeiites from the Oceanographer Fracture Zone, *Contrib. Mineral. Petrol.*, *70*, 111–125.
- Weaver, J., and C. H. Langmuir (1990), Calculation of phase equilibrium in mineral-melt systems *Comp. Geosci.*, *16*, 1–19.
- Yang, H.-J., R. J. Kinzler, and T. L. Grove (1996), Experiments and models of anhydrous, basaltic olivine-plagioclase-augite saturated melts from 0.001 to 10 kbar, *Contrib. Mineral. Petrol.*, *124*, 1–18.
- Yi, W., A. N. Halliday, J. C. Alt, D. C. Lee, M. Rehkämper, M. O. Garcia, and Y. J. Su (2000a), Cadmium, indium, tin, tellurium, and sulfur in oceanic basalts: Implications for chalcophile element fractionation in the Earth, *J. Geophys. Res.*, *105*, 18,927–18,948.
- Yi, W., A. Halliday, J. Alt, D. Lee, M. Rehkämper, M. Garcia, C. Langmuir, and Y. Su (2000b), Erratum: “Cadmium, indium, tin, tellurium, and sulfur in oceanic basalts: Implications for chalcophile element fractionation in the Earth,” *J. Geophys. Res.*, *105*, 23,761–23,762.
- Yoder, H. S., and C. E. Tilley (1962), Origin of basaltic magmas: Experimental study of natural and synthetic rock systems, *J. Petrol.*, *3*, 342–532.